Multiscale Modeling of the Mechanical Behaviour of Pearlitic Steel

E. Lindfeldt, M. Ekh

Pearlitic steel is a two-phase material with cementite lamellae embedded in a ferrite matrix. In this contribution a representative microscale model, capturing the behavior of the cementite and the ferrite and also the interaction between these phases, is proposed. The response from the micromodel is coupled by means of computational homogenization to a representative mesomodel containing grains, or colonies, of pearlite. The material parameters of the ferrite and the cementite are identified by calibrating the model to experimental data for the pearlitic steel R260. Different types of prolongation conditions, i.e. how to couple the mesoscale kinematics to the microscale kinematics, are investigated and their results are compared. Finally, the influence of the number of cementite directions and the number of crystallographic orientations on the macroscopic stress response is studied. Thereby, a sufficient mesomodel size is estimated.

1 Introduction

Pearlitic steels are used to produce for example springs and wires. These applications are often produced through wire drawing. In this process the desired mechanical properties are achieved by changes in the microstructure caused by the repeated area reductions. Another example of application is rail. In the contact between the train wheel and the rail high contact forces (both frictional and normal) appear. These forces tend to align the micro structure so that the mechanical behavior and also the fracture properties of the rail are affected.

Pearlite is a two-phase material with hard and brittle cementite lamellae embedded in a ferrite matrix. Using the definition of Mehl (1948) these lamellae are arranged in colonies within which the orientation of the cementite is (ideally) constant. The typical geometrical quantities on this scale all depend on the pertinent heat treatment. The pearlite colony size lies within the range (see Elwazri et al. (2005)) $4.5\mu m \leq t_{PC} \leq 7.8\mu m$ while the cementite lamellae thickness varies within $0.015\mu m \leq t_C \leq 0.030\mu m$.

Over the years, material scientists have studied the relation between microstructural quantities and macroscopic properties. A classical example is the work done by Hall (1951) and Petch (1953) who studied the relation between the macroscopic yield stress and the grain (pearlite colony) size. A more recent example is the work done by Toribio and Ayaso (2003) who studied the effect on the stress-strain curve of an increasing alignment of the microstructure.

When it comes to the modeling of a pearlitic steel many macroscopic models of varying complexity are available (see e.g. the work by Hu et al. (2006), Johansson and Ekh (2006) and Johansson et al. (2006)). These could include several hardening mechanisms and complex yield criteria. The complexity of the model is reflected in the number of parameters needed to quantify the material behavior. These parameters must be identified, based on experimental results, for each variation of the material.

By using the concept of computational homogenization (see e.g. Feyel and Chaboche (2000) and Miehe et al. (1999)) the microstructure of the material can be taken into account explicitly. The macroscopic behavior of the model is then linked to a sub-scale model within which the heterogeneities of the material are accounted for. This is done by finite element modeling of a Representative Volume Element (RVE) of the microstructure.

An attempt to model pearlite along the lines described above was done by Long et al. (2008) who considered the average response of an RVE using analytical averaging of the combined response of the constituents. In the present contribution this anzatz is extended by considering the response from a finite element discretized RVE, and for the ferrite a crystal plasticity model is used which is formulated within the framework of finite deformations while Long et. al. assume that the strains are small.

In the current contribution the proposed multiscale modeling framework employs three scales where the mesoscale domain is used to study interactions between "grains", i.e. regions with different material orientations. Rather than coupling this scale to a constitutive model it is linked to the homogenized response of a microscale model which simulates the interactions between the constituents. This multiscale setup is very similar to the one suggested

by Kouznetsova and Geers (2008). However, there it was used to study the effect of phase transformations in martensitic steels.

This paper is arranged as follows. In Section 2 the multiscale modeling framework is outlined. This includes possible choices for boundary conditions as well as a description of the resulting FE-algorithm. In Section 3 the details of the chosen constitutive framework are summarized together with a description of the corresponding numerical treatment. Finally, in Section 4 some numerical results are presented showing the effect of varying the orientations on the microscale as well as examples showing the influence of the boundary conditions on the micro model.

2 Multiscale Modeling Framework

In the present section the details of the multiscale modeling framework used in the present study will be outlined. This includes a subsection on the boundary conditions and the corresponding homogenization scheme. Furthermore, the pertaining FE-algorithm is discussed in subsection 2.3.

2.1 Scales

Within the present modeling framework three different scales, see Figure 1, are used to capture the mechanisms of interest. The macroscale domain, $\bar{\Omega}$, is where the behaviour of a typical engineering component is studied by solving the equilibrium equation (assuming quastistatic conditions and no body forces), in terms of the 1st Piola-Kirchhoff stress, $\text{Div}(\bar{\mathbf{P}}) = \mathbf{0}$ with proper boundary conditions. The relation between the macroscopic stress, $\bar{\mathbf{P}}$ and the corresponding deformation gradient, $\bar{\mathbf{F}}$, is governed by the mesomodel.

It is well known (see for example Toribio and Ayaso (2003) or Wetscher et al. (2007)) that changing the size and/or shape of the pearlite colonies will have consequences on the macroscale behavior of the pearlite. Such effects can be captured by the modeling of a mesoscopic domain, $\hat{\Omega}$. As is schematically illustrated in Figure 1 the model contains a number of colonies where the cementite orientation and the crystallographic orientation of the constituents may vary. Also on the mesoscale we must, in the general case, find the equilibrium state by solving the equilibrium equation, $\text{Div}(\hat{\mathbf{P}}) = \mathbf{0}$, together with the appropriate boundary conditions. On this scale it is the microscale model that defines the relation between the mesostress, $\hat{\mathbf{P}}$, and the mesoscopic deformation gradient, $\hat{\mathbf{F}}$.

In order to explicitly take into account the interactions between the constituents of pearlite, the microscale (denoted Ω) is introduced. Here, properties such as volume fractions and shapes of the constituents can be varied. Based on the idealized assumption that the cementite orientation is constant within a colony, the micromodel is modeled in a periodic fashion. The microscale displacements are found by solving the equilibrium equation $\text{Div}(\mathbf{P}) = \mathbf{0}$ for a suitable choice of boundary conditions. The behavior of the constituents, in terms of $\mathbf{P}$ as a function of $\mathbf{F}$, is governed by the chosen constitutive models which are described in Section 3.

Furthermore, in order to model different cementite lamellae directions we transform the components of the mesoscale deformation gradient $\hat{\mathbf{F}}$ using a coordinate transformation to a local coordinate system of the micromodel. Consequently, the components of the obtained stress response, $\hat{\mathbf{P}}$ must be transformed back to the coordinate system of the mesomodel.

Having established the behavior of the different scales it now remains to show how the scales are linked via the choices of displacement boundary conditions and the pertaining homogenization scheme. The details thereof will be presented in the next section.

In the following we will restrict the modeling to the meso- and microscale, i.e. it will be assumed that the macroscopic deformation gradient, $\bar{\mathbf{F}}$, is known.
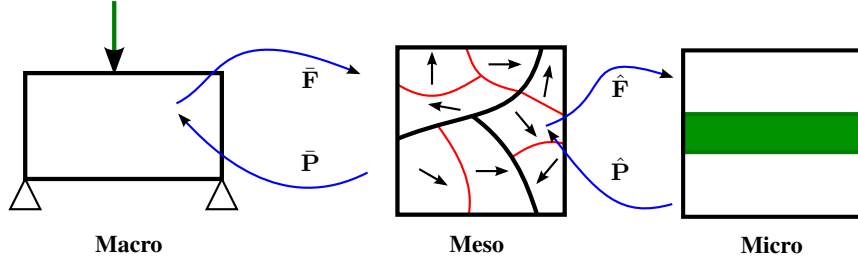
Figure 1: Scales considered in the multiscale framework

2.2 Prolongation Conditions and Homogenization

In a multiscale modeling framework the communication between the scales is governed by the choice of prolongation conditions and the thereby resulting homogenization scheme, see e.g. Hill (1963). In a kinematically driven framework a natural choice is to use the deformation gradients, $\bar{\mathbf{F}}$ and $\hat{\mathbf{F}}$ to impose the chosen prolongation conditions on the fluctuation fields $\hat{\mathbf{w}} = \hat{\mathbf{x}} - \bar{\mathbf{F}} \cdot \hat{\mathbf{X}}$ and $\mathbf{w} = \mathbf{x} - \hat{\mathbf{F}} \cdot \mathbf{X}$. Table 1 summarizes the field equations and three possible choices of prolongation conditions for the mesoscale and the microscale.

Table 1: Field equations and prolongation conditions

Domain	Mesoscale	Microscale
Field eq.	$\mathrm{Div}(\hat{\mathbf{P}}) = \mathbf{0}$	$\mathrm{Div}(\mathbf{P}) = \mathbf{0}$
Taylor	$\hat{\mathbf{w}} = 0 \ \forall \hat{\mathbf{X}} \in \hat{\Omega}$	$\mathbf{w} = 0 \ \forall \mathbf{X} \in \Omega$
Dirichlet	$\hat{\mathbf{w}} = 0 \ \forall \hat{\mathbf{X}} \in \partial\hat{\Omega}$	$\mathbf{w} = 0 \ \forall \mathbf{X} \in \partial\Omega$
Periodic	$\hat{\mathbf{w}}^{+} = \hat{\mathbf{w}}^{-} \ \forall \hat{\mathbf{X}} \in \partial\hat{\Omega}^{+}$	$\mathbf{w}^{+} = \mathbf{w}^{-} \ \forall \mathbf{X} \in \partial\Omega^{+}$

Clearly, the Taylor assumption is more restrictive than a displacement boundary condition and it has the advantage that no field equation needs to be solved. Instead, there is only one call to the constitutive driver per constituent. In the case of periodic boundary conditions the tractions must also fulfill, due to the assumption of periodicity, $\hat{\mathbf{p}}^{+} + \hat{\mathbf{p}}^{-} = \mathbf{0} \ \forall \ \hat{\mathbf{X}} \in \partial\hat{\Omega}^{-}$ and $\mathbf{p}^{+} + \mathbf{p}^{-} = \mathbf{0} \ \forall \ \mathbf{X} \in \partial\Omega^{-}$. For these three prolongation conditions the Hill-Mandel (see e.g. Hill (1963)) criterion gives that $\bar{\mathbf{P}} = \frac{1}{V(\hat{\Omega})} \int_{\hat{\Omega}} \hat{\mathbf{P}} \mathrm{d}\hat{\Omega}$ and $\hat{\mathbf{P}} = \frac{1}{V(\Omega)} \int_{\Omega} \mathbf{P} \mathrm{d}\Omega$.

2.3 FE-Algorithm

In this section the FE-algorithm will be presented together with the chosen iterative scheme that is used to solve the non-linear FE-problem. For brevity only the microscale equations are showed. However, the reasoning is the same for the mesoscale.

By using Galerkin's method in a standard fashion, the weak form of the equilibrium equation is used to obtain the FE-unbalances as

$$\underline{f}(\underline{a}) = \int_{\Omega} (\mathbf{P} : \nabla_0 \underline{N}) \mathrm{d}\Omega = \underline{0}. \tag{1}$$

In this equation $\underline{a}$ is introduced as the nodal degrees of freedom so that they together with the shape functions $\underline{N}$ give the approximate displacement field $\mathbf{u} \approx \mathbf{u}^{h} = \underline{N} \cdot \underline{a}$.

When using Dirichlet boundary conditions the nodes are partitioned into internal nodes i and boundary nodes p, c.f. Figure 2a. The independent degrees of freedom are then updated in a Newton iteration according to

$$^{k}\underline{a}^{i} = {}^{k-1}\underline{a}^{i} - \left(\frac{\partial \underline{f}^{i}}{\partial \underline{a}^{i}}\right)^{-1} : {}^{k-1}\underline{f}^{i} \tag{2}$$
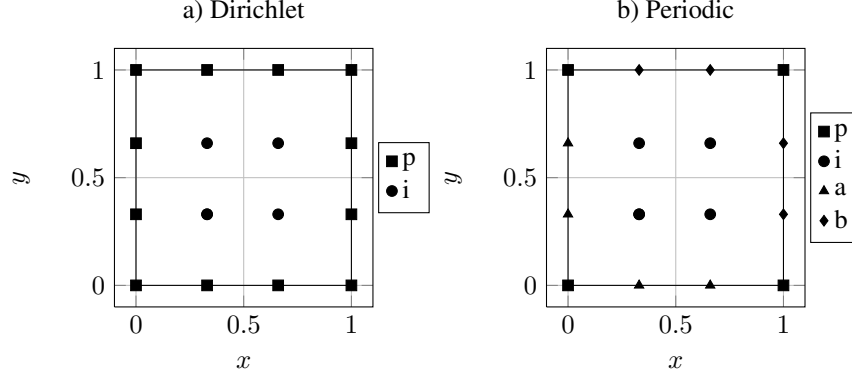
until convergence has been reached.

Figure 2: Partitioning of nodes for a) Dirichlet boundary conditions b) periodic boundary conditions

In the case where periodic boundary conditions are used a different partitioning of the nodes is used, see Figure 2b. The difference is that the boundary nodes are are divided into three sets; the corner nodes p, the nodes on the positive boundary a and the corresponding nodes on the negative boundary b. The position of the corner nodes can be calculated a priori based on the assumed periodicity of the fluctuations $\mathbf{w}^+ = \mathbf{w}^-$ while the remaining nodes are treated as independent and solved for using the modified FE-unbalances

$$\underline{f}^f_{per} = \begin{bmatrix} \underline{f}^i_{per} \\ \underline{f}^a_{per} \\ \underline{f}^b_{per} \end{bmatrix} = \begin{bmatrix} \underline{f}^i \\ \underline{a}^a - \underline{a}^b + \underline{c} \\ \underline{f}^a + \underline{f}^b \end{bmatrix} = \underline{0} \tag{3}$$

where the constant vector $\underline{c}$ is introduced so that the matrix equation $\underline{a}^a - \underline{a}^b + \underline{c} = \underline{0}$ corresponds to $\mathbf{w}^a = \mathbf{w}^b \Leftrightarrow \mathbf{u}^a - (\hat{\mathbf{F}} - \mathbf{I})\mathbf{X}^a = \mathbf{u}^b - (\hat{\mathbf{F}} - \mathbf{I})\mathbf{X}^b$. Once again the independent nodal values are iteratively solved for in a Newton iteration

$$^k\underline{a}^f = {}^{k-1}\underline{a}^f - \left(\frac{\partial \underline{f}^f_{per}}{\partial \underline{a}^f} \right)^{-1} : {}^{k-1}\underline{f}^f_{per} \tag{4}$$

until convergence has been reached.

3   Constitutive Model

The constitutive equations used for the modeling of the ferrite and the cementite in the micromodel are summarized below. The deformation gradient $\mathbf{F}$ is split multiplicatively such that the elastic part of the deformation gradient $\mathbf{F}_e = \mathbf{F} \cdot (\mathbf{F}_p)^{-1}$,where $\mathbf{F}_p$ is the plastic part of the deformation gradient, is used to define the elastic response of Neo-Hooke type according to

$$\mathbf{S}_e = \frac{\lambda}{2}(\text{tr}\,\mathbf{C}_\mathrm{e} - 3)\mathbf{I} + \mu(\mathbf{C}_\mathrm{e} - \mathbf{I}) \tag{5}$$

where $\mathbf{C}_\mathrm{e} = \mathbf{F}_\mathrm{e}^\mathrm{T} \cdot \mathbf{F}_\mathrm{e}$. In this equation $\mathbf{S}_e$ is the elastic 2nd Piola-Kirchhoff stress and λ and μ are the Lamé constants. From $\mathbf{S}_e$ other stress measures such as the Kirchhoff stress $\tau = \mathbf{F}_e \cdot \mathbf{S}_e \cdot \mathbf{F}_e^\mathrm{T}$ and the Mandel stress $\mathbf{M} = \mathbf{C}_e \cdot \mathbf{S}_e$ can be obtained.

The cementite is assumed to behave elastically and is modeled by the same type of Neo-Hooke elasticity (with $\mathbf{F}_\mathrm{p} = \mathbf{I}$ and hence $\mathbf{C}_\mathrm{e} = \mathbf{F}^\mathrm{T} \cdot \mathbf{F}$).

For the inelastic response of the ferrite a crystal plasticity model, based on the work of Hill and Havner (1982), Havner (1992), Asaro (1983), Kocks (1970), Kocks (1975), Hutchinson (1970) and Lubarda (1999), is used. Further details about the model can be found in Ekh et al. (2004).

The Mandel stress tensor $\mathbf{M}$ can now be used to compute the resolved (Schmid) stress τ_α on slip system α according to

$$\tau_\alpha = \mathbf{s}_\alpha \cdot \mathbf{M} \cdot \mathbf{m}_\alpha \tag{6}$$

where $\mathbf{s}_\alpha$ and $\mathbf{m}_\alpha$ are the slip plane direction and the slip plane normal, respectively. Note that $\mathbf{s}_\alpha$ and $\mathbf{m}_\alpha$ are defined in the intermediate configuration but are assumed (isoclinic assumption) to be equal to the corresponding vectors in the undeformed configuration. The dyadic product $\mathbf{s}_\alpha \otimes \mathbf{m}_\alpha$ defines slip system α. The Schmid stress is then used in the yield function Φ_α

$$\Phi_\alpha = |\tau_\alpha| - [Y_\alpha + \kappa_\alpha] \tag{7}$$

where κ_α is the hardening stress and Y_α is the initial yield stress. The formulation and evolution of the hardening stress κ_α is chosen in accordance with Chang and Asaro (1981) as

$$\dot{\kappa}_\alpha = \sum_{\beta=1}^{Nslip} \left(q + [1 - q]\, \delta_{\alpha\beta} \right) h_\beta(A_\beta) \dot{\gamma}_\beta \tag{8}$$

$$h_\alpha(A_\alpha) = h_0 + [h_\infty - h_0]\left[1 - \exp\left(-\xi A_\alpha\right)\right] \tag{9}$$

$$A_\alpha = \sum_{\beta=1}^{N_{slip}} [q + [1 - q]\, \delta_{\alpha\beta}]\, \gamma_\beta \tag{10}$$

Here, q controls the degree of self- and cross-hardening, ξ influences the non-linearity of the hardening evolution, h_0 is the initial hardening modulus and h_∞ is the saturation hardening modulus. The variable that controls the hardening is the plastic slip γ_α. The evolution of plasticity follows an associated format (see e.g. Simo (2004))

$$\mathbf{l}_p = \sum_{\alpha=1}^{N_{slip}} \dot{\gamma}_\alpha \frac{\partial \Phi_\alpha}{\partial \mathbf{M}} = \sum_{\alpha=1}^{N_{slip}} \dot{\gamma}_\alpha \, \mathrm{sgn}(\tau_\alpha) \mathbf{s}_\alpha \otimes \mathbf{m}_\alpha \tag{11}$$

where $\mathbf{l}_\mathrm{p}$ is the plastic rate of deformation tensor. In a true rate-independent plasticity the plastic slip is determined from the loading/unloading conditions

$$\Phi_\alpha \leq 0 \, , \ \dot{\gamma}_\alpha \geq 0 \, , \ \dot{\gamma}_\alpha \cdot \Phi_\alpha = 0. \tag{12}$$

However, to avoid difficulties with non-uniqueness (see e.g. Miehe et al. (1999)) of the solution a regularization via a Perzyna type of viscoplasticity is adopted, i.e.

$$\dot{\gamma}_\alpha = \frac{1}{t_*} \eta_\alpha(\Phi_\alpha) = \frac{1}{t_*} \left(\left[\frac{\langle \Phi_\alpha \rangle}{Y_\alpha + \kappa_\alpha} + 1 \right]^{n_\alpha} - 1 \right). \tag{13}$$

In this equation t_* is the relaxation time and n_α is the overstress exponent.

Depending of the type of crystal structure that is to be studied different families of slip systems are possible. In the current contribution only the ferrite domain is treated as plastic. In a pearlitic steel the ferrite atoms are arranged in a body centered cubic structure (see e.g. Zhou and Shiflet (1992)).

For this type type of α-Fe three families of slip systems could be active (see e.g. Callister (2003)); $\{110\}\langle\bar{1}11\rangle$, $\{211\}\langle\bar{1}11\rangle$ and $\{321\}\langle\bar{1}11\rangle$. The first two families contain 12 slip systems each while the third comprises 24 slip systems. Adding more slip systems to the model increases the number of internal variables and hence makes the model more computationally demanding. For this reason, the 12 slip systems of the $\{110\}\langle\bar{1}11\rangle$ family are chosen. The corresponding slip planes and directions are listed in Table 2.

Table 2: Slip systems

α	1	2	3	4	5	6
$\mathbf{m}_\alpha$	(011)	(011)	$(01\bar{1})$	$(01\bar{1})$	(101)	(101)
$\mathbf{s}_\alpha$	$[11\bar{1}]$	$[1\bar{1}1]$	$[111]$	$[\bar{1}11]$	$[11\bar{1}]$	$[\bar{1}11]$
α	7	8	9	10	11	12
$\mathbf{m}_\alpha$	$(\bar{1}01)$	$(\bar{1}01)$	(110)	(110)	$(1\bar{1}0)$	$(1\bar{1}0)$
$\mathbf{s}_\alpha$	$[111]$	$[1\bar{1}1]$	$[1\bar{1}1]$	$[\bar{1}11]$	$[111]$	$[11\bar{1}]$

3.1 Time Integration of the Constitutive Equations

The evolution equations are integrated numerically using the backward Euler rule. As described in Ekh et al. (2004) (here without crystallographic damage) the arising nonlinear equations become

$$\mathbf{R}_{\mathbf{F}_p} = (\mathbf{F}_p - {}^n\mathbf{F}_p)\mathbf{F}_p^{-1} - \sum_{\alpha=1}^{N_{slip}} \Delta\gamma_\alpha \mathbf{s}_\alpha \otimes \mathbf{m}_\alpha = \mathbf{0} \tag{14}$$

$$R_{\kappa_\alpha} = \kappa_\alpha - {}^n\kappa_\alpha - \sum_{\beta=1}^{Nslip} \left(q + [1-q]\, \delta_{\alpha\beta} \right) h_\beta(A_\beta)\Delta\gamma_\beta = 0 \tag{15}$$

$$R_{\Delta\gamma_\alpha} = \Delta\gamma_\alpha - \frac{\Delta t}{t_*}\eta_\alpha(\Phi_\alpha) = 0 \tag{16}$$

Clearly, it is possible to reduce the unknowns to only $\Delta\gamma_\alpha$ since both $\mathbf{F}_p$ and κ_α can be written explicitly in terms of $\Delta\gamma_\alpha$. The unknowns $\Delta\gamma_\alpha$ are solved by Newton iterations.

3.2 Plane Stress Iteration

In the numerical examples in Section 4 the plane stress assumption will be adopted. The plane stress condition is assumed to be local in every (Gauss) point of the micromodel. To be specific, in a Cartesian coordinate system we assume that the stresses in the $\bar{\mathbf{e}}_3$ direction are zero. This means that the components $\bar{P}_{i3}$ of the 1st Piola-Kirchhoff stress must be zero. To obtain this we iterate on the corresponding components of the deformation gradient, i.e. $\bar{F}_{i3}$ using Newton iterations.

4 Numerical Examples

Before proceeding with the numerical examples the model is calibrated against experimental data for the pearlitic steel R260 from Ahlström and Karlsson (2005). The experimental data comes from a uniaxial stress test. In order to resemble the test conditions the in-plane components of the macroscopic deformation gradient $\bar{\mathbf{F}}$ are prescribed according to Table 3

Table 3: Loading used in the calibration

Load case	F_{11}	F_{12}	F_{21}	F_{22}
Calibration	$1+\gamma$	0	0	$1-\nu\cdot\gamma$

where ν is Poisson's ratio and γ is the loading parameter. This loading together with the plane stress assumption yields conditions similar to the experimental setup. Using a calibration algorithm based on both simplex and gradient optimization (see e.g. Lundgren et al. (2010)) a set of parameters giving a reasonable agreement with the experimental results was found, see Figure 3.

During the calibration a mesomodel based on the Taylor assumption is used (i.e. $\hat{\mathbf{w}} = \mathbf{0}\ \forall\hat{\mathbf{X}} \in \hat{\Omega}$) with 4 crystallographic orientations and 2 cementite orientations which are combined to give 8 unique sets of orientations. Furthermore, Dirichlet boundary conditions are used for the micromodel with geometry and discretization according to G10M01 in Figure 4.

Clearly, the set of material parameters would change when using other meso- and micromodels. Nevertheless, with the identified material parameters we have a reasonable and realistic model behavior as compared to the pearlitic steel R260.
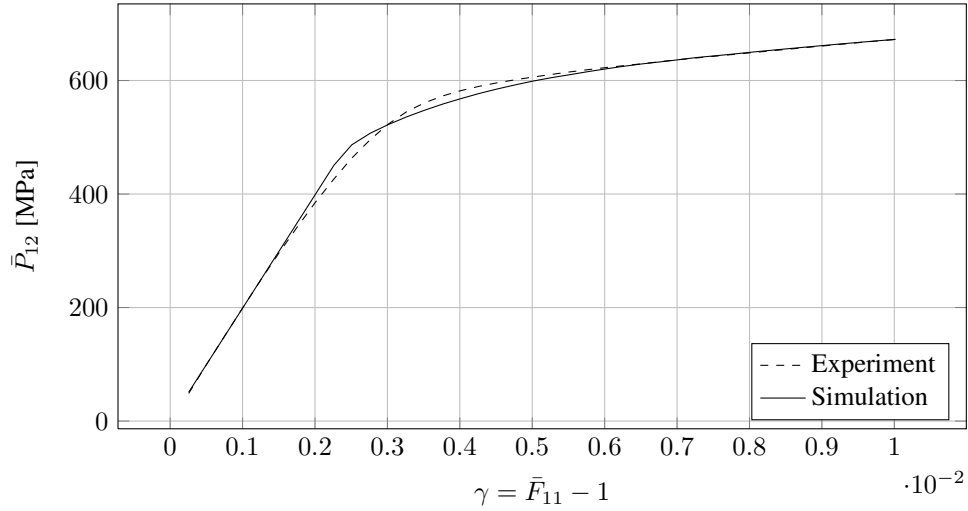
Figure 3: Comparison between experimental data (dashed) for the pearlitic steel R260 and simulation (solid) with identified material parameters

The identified parameters are listed in Table 4. For the cementite only the elastic properties are listed.

Table 4: Identified material parameters

Material	E [GPa]	ν	$Y_\alpha [MPa]$	q	h_0 [MPa]	h_∞ [MPa]	ξ	t_* [s]	n_α
Ferrite	198	0.3	190	1.5	8400	0	190	100	1
Cementite	198	0.3							

In order to study the behaviour of the present model a number of numerical examples are carried out. In particular, the influence of the number of crystallographic directions in the ferrite, the number of colonies (cementite lamellae directions), the size of the micromodel and the boundary conditions used for the micromodel are investigated. These investigations are limited to 2D modeling using a plane stress assumption (see Subsection 3.2) in the micromodel and also by only allowing in-plane variations of the orientations.

For all of these examples the material parameters identified during the calibration, see Table 4, are used. In these examples two load cases, 2D elongation and simple shear, are used to quantify the model behavior, see Table 5. On the mesolevel the Taylor assumption, i.e. $\hat{\mathbf{F}} = \bar{\mathbf{F}}$ is used.

Table 5: Load cases considered in the numerical examples

Load case	$\bar{F}_{11}$	$\bar{F}_{12}$	$\bar{F}_{21}$	$\bar{F}_{22}$
2D elongation	$1 + \gamma$	0	0	$(1 + \gamma)^{-1}$
Simple shear	1	γ	0	1

When studying the effect on the mesoscopic stress response of varying the size of the micromodel (in terms of the number of cementite lamellae) and also the mesh resolution a number of different FE models are used. These models are showed in Figure 4.
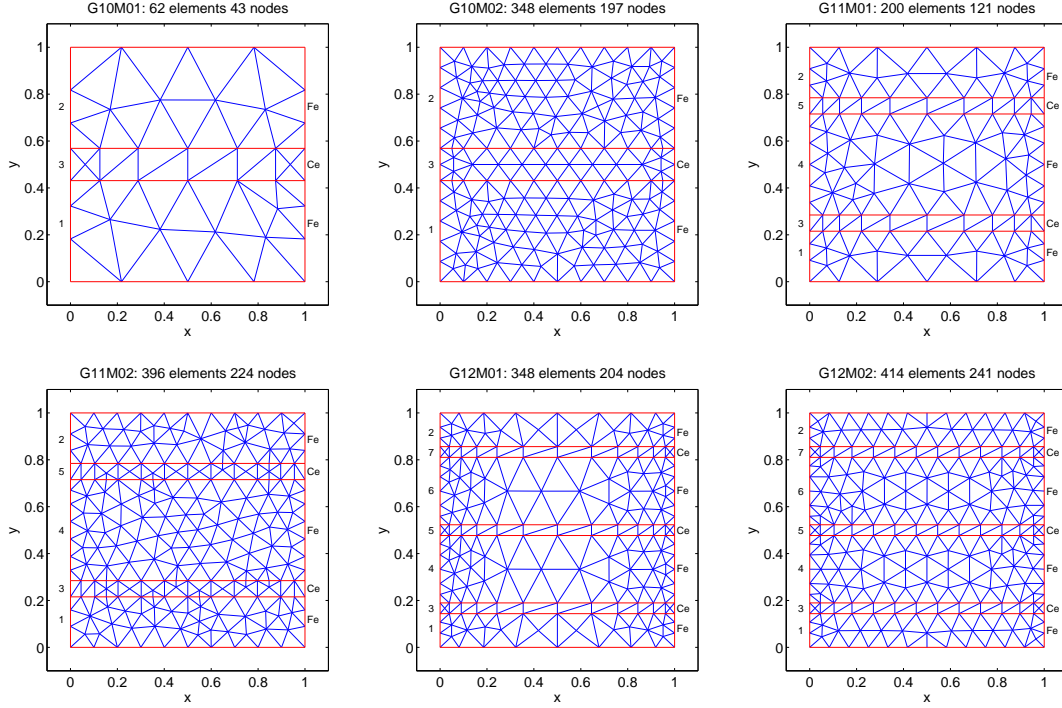
Figure 4: Micromodels used in the numerical examples, with 1 (G10M01 and G10M02), 2 (G11M01 and G11M02) and 3 (G12M01 and G12M02) cementite lamellae.

4.1 Investigation of the Crystallographic Anisotropy

As a means to quantify the significance of the crystal orientation a single phase domain of ferrite (using the corresponding material parameters listed in Table 4) is considered. The mesoscopic stress response for a number of mesograins with varying crystal orientation is studied. In the current example 16 grains with a crystal orientation angle $\varphi_1^i = 0° + (i-1) \cdot 90°/16$ where $i = 1, \ldots, 16$.

In Figure 5a the response from a simple shear type of loading is plotted. Among the individual responses a large spread depending on the current value of φ_1 can be observed.
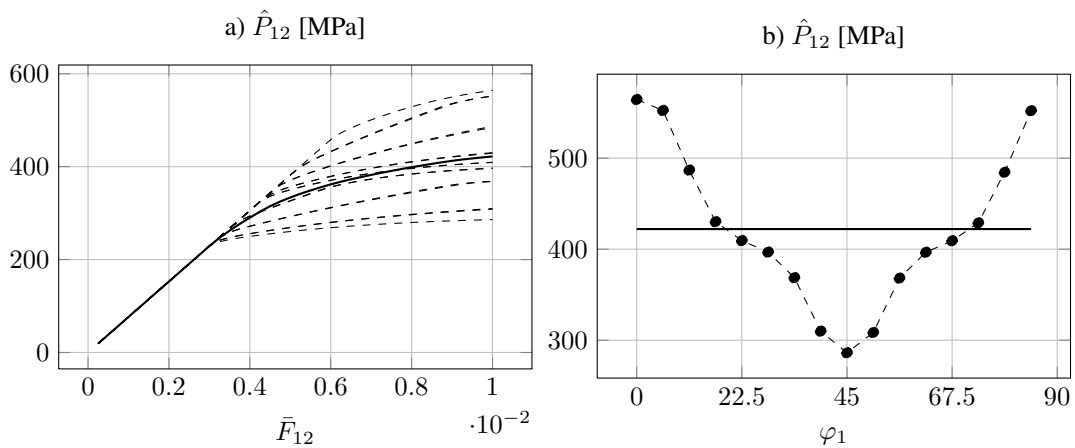
Figure 5: Simple shear, individual responses (dashed) in terms of $\hat{P}_{12}$ and average response (solid) plotted: a) as function of $\bar{F}_{12}$; b) as function of φ_1 evaluated at $\bar{F}_{12} = 0.01$

For a 2D elongation type of loading similar results are observed, see Figure 6.
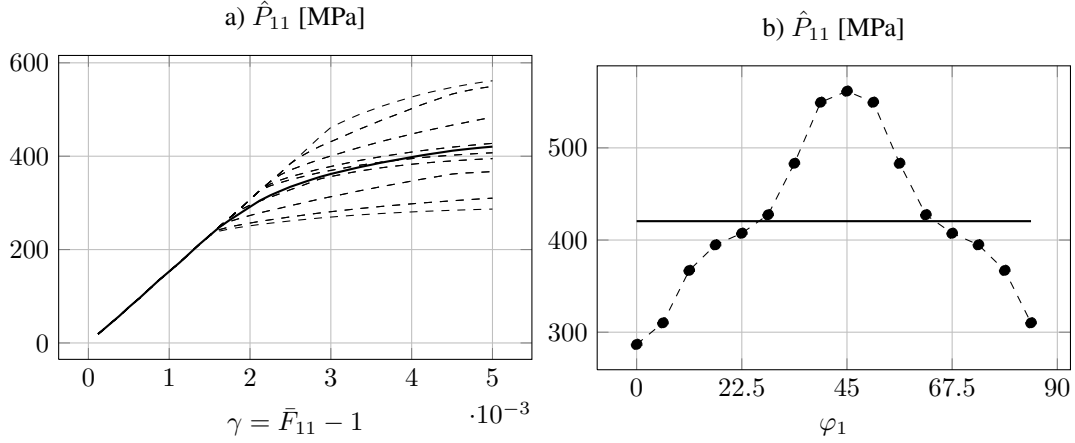
Figure 6: 2D elongation, individual responses (dashed) in terms of $\hat{P}_{11}$ and average response (solid) plotted: a) as function of $\bar{F}_{11}$; b) as function of φ_1 evaluated at $\bar{F}_{11} = 1.005$

From these results it is clear that the behavior of the ferrite domain, with the current set of slip systems (see Table 4), indeed depends on the crystal orientation. The issue of how many crystal orientations are needed to obtain a representative response will be addressed in Subsection 4.4.

By observing how the response depends on the crystal orientation it might be tempting to assume that the results are symmetric about $45°$. However, the numerical values of the other stress components show (although values are not presented here) that the symmetry plane is, as expected, at $90°$.

4.2 Anisotropy of the Chosen RVE

Having established the significance of altering the crystal orientation, the anisotropy of the micromodel will now be studied by comparing the stress response from micromodels with different cementite orientations. To this end the mesograins are assigned cementite orientations $\theta_1^j = 0 + (j - 1) \cdot 180°/N_{\theta_1}$ where $N_{\theta_1} = 16$ is the chosen number of different cementite orientations and $j = 1, \ldots, N_{\theta_1}$.

For the simple shear load case, the responses from the micromodels are showed in Figure 7. From these results it is noted that the influence on the stress response of varying the cementite angle does not give as strong influence on the stress response as varying the crystal orientation cf. Figure 5.
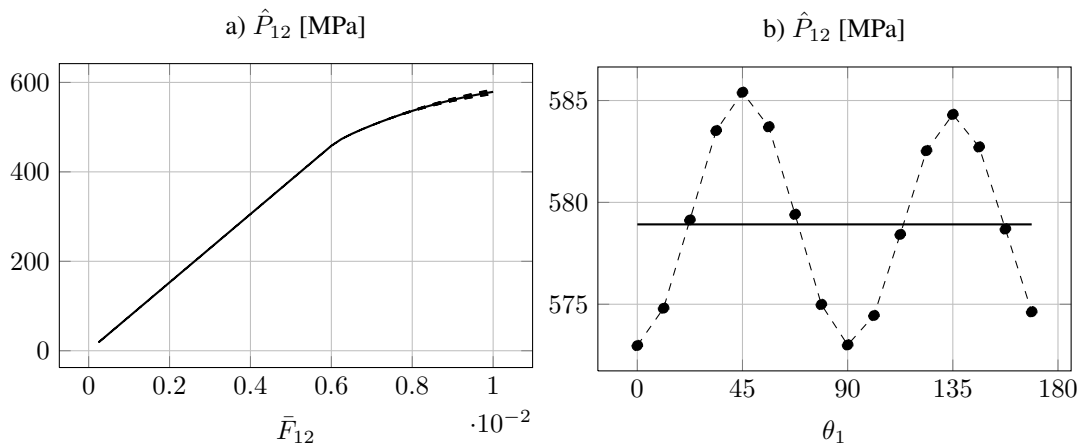

Figure 7: Simple shear, individual responses (dashed) in terms of $\hat{P}_{12}$ and average response (solid) plotted a) as function of $\bar{F}_{12}$, b) as function of θ_1 evaluated at $\bar{F}_{12} = 0.01$

If the attention instead is given to the 2D elongation load case then the stress responses showed in Figure 8 are obtained.
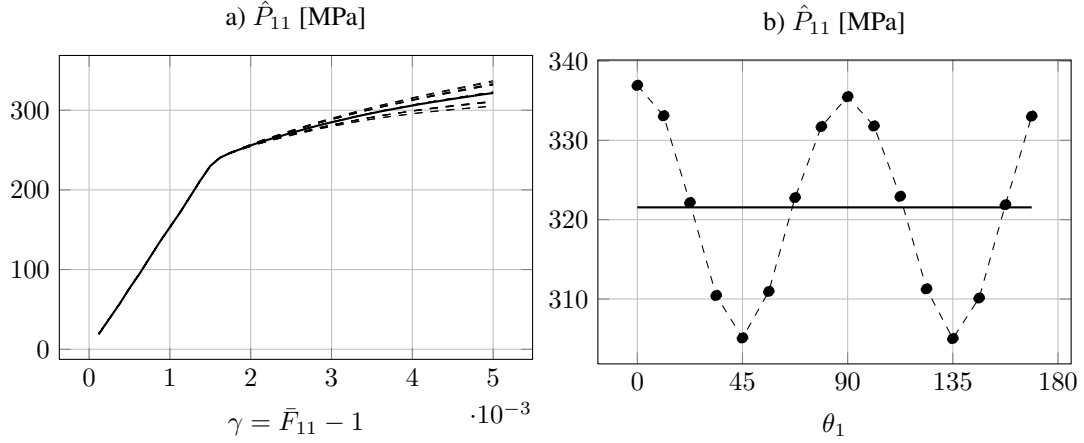
388

Figure 8: 2D elongation, individual responses (dashed) in terms of $\hat{P}_{11}$ and average response (solid) plotted a) as function of $\bar{F}_{11}$, b) as function of θ_1 evaluated at $\bar{F}_{11} = 1.005$

Although the influence from varying the cementite orientation is slightly larger for this load case, we can still conclude that the influence from varying the cementite orientation is smaller than the influence from varying the crystallographic orientation of the ferrite. Also in the present example it might seem as if a symmetry is obtained about $\theta_1 = 90°$. However, similarly as in Subsection 4.1 the other stress components (not presented here) show that the symmetry is, as expected, located about $\theta_1 = 180°$.

4.3 Size of Micromodel

In this subsection we study the effects of changing the number of cementite lamellae and the mesh resolution in the micromodel as well as changing the boundary conditions used to transfer the kinematics from the mesoscale to the microscale. To do so, 6 different micro-RVE:s are considered which have 1, 2 or 3 lamellae and two different mesh resolutions, see Figure 4.

The mesoscopic responses in terms of the stress component $\hat{P}_{11}$ for the 2D elongation load case are plotted in Figure 9. In this figure M01 denotes responses from coarse meshes and M02 denotes the responses from slightly refined meshes.
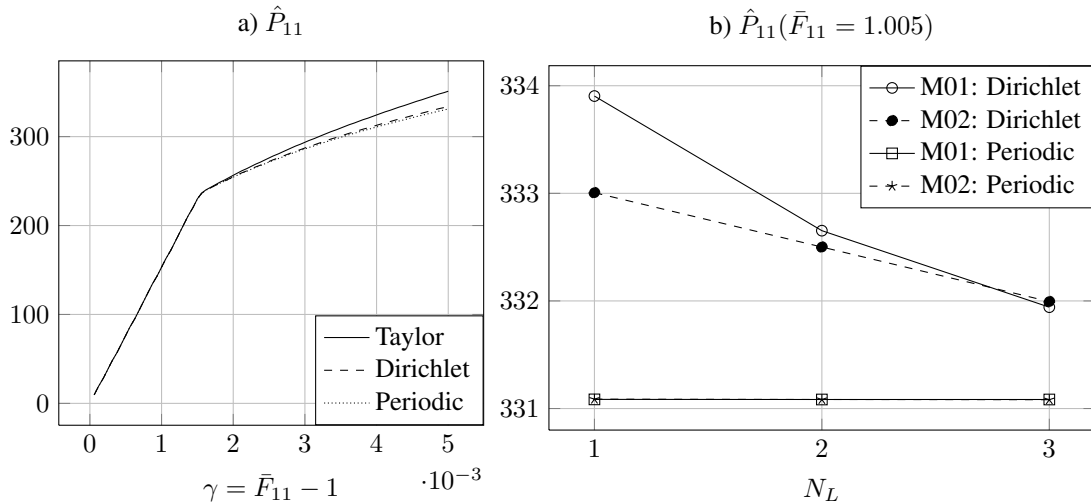

Figure 9: Mesoscopic stress response in terms of $\hat{P}_{11}$. a) as a function of $\bar{F}_{11}$, using the micro-RVE G10M01, for three different boundary conditions b) evaluated at $\bar{F}_{11} = 1.005$ plotted as function of the number of lamellae for different mesh resolutions and varying boundary conditions.

From Figure 9 it is observed that, as expected, the Taylor assumption gives the stiffest response. Furthermore, also expectedly, the Dirichlet boundary conditions are stiffer than the periodic boundary conditions. It is also noted that

the periodic boundary condition is very independent of what mesh is used.

Therefore, the overall conclusion is that the periodic boundary condition is the preferable choice since it allows for the simplest micro-RVE to be used and thus provides the most computationally efficient model.

However, if the loads are close to the yield limit it might be wise to consider the Taylor assumption due to the significant reduction of computational costs which is obtained since no FE-problem needs to be solved.

4.4 Size of Mesomodel

It has been showed in the previous subsections that the mesoscopic response, i.e. the homogenized microscopic response, depends both on the chosen orientation of the crystal and on the cementite lamella orientation. Therefore, it is interesting to study the influence of the number of orientations (both cementite and crystallographic) on the resulting stress response.

In Figure 10 the macroscopic stress response for the two considered load cases is plotted as a function of the number of crystal- and cementite orientations which are included in the mesomodel.
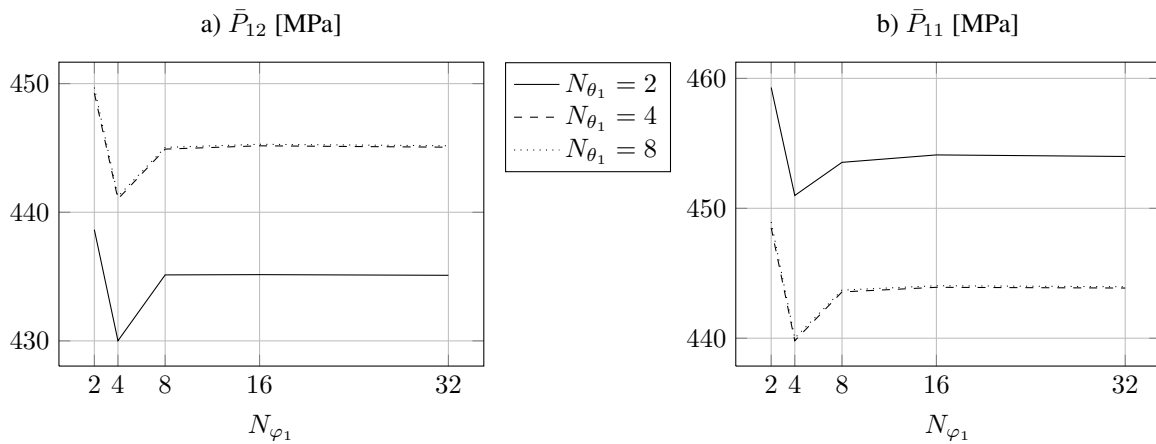

Figure 10: Macroscopic stress response for a varying number of included orientations. a) Simple shear evaluated at $\mathbf{F}_{12} = 0.01$. b) 2D elongation evaluated at $\mathbf{F}_{11} = 1.005$.

From Figure 10 it can be observed that the macroscopic stress response is rather insensitive to the number of cementite orientations, N_{θ_1}. To include more than 4 orientations does not have any impact on the macroscopic stress response. However, when it comes to the number of crystal orientations, N_{φ_1}, it seems to be necessary to include at least 16 orientations.

In total, this means that a 2D representative mesomodel should include 4 cementite orientations and 16 crystal orientations resulting in 64 unique combinations of orientations.

5 Concluding Remarks

A representative, 2-dimensional, multiscale model of a fully pearlitic steel has been presented. The model features two scales, each of which representing different mechanisms. The scales are coupled by the means of computational homogenization. The mesomodel comprises colonies ("grains") with different orientations of the cementite lamellae and also varying crystallographic orientations of the ferrite. In the microscale model the behavior of the constituents (using a crystal plasticity model for the ferrite and elasticity for the cementite) is taken into account and also the interactions between them. The proposed model has been calibrated to experimental data and together with the identified material parameters the model response shows a good correlation to the experimental data. By varying the crystallographic orientation of the ferrite it has been shown that this has a strong impact on the homogenized stress response. Similarly, by varying the cementite orientation and observing the corresponding impact on the stress response it was noted that this effect is smaller than the corresponding effect caused by varying the crystallographic orientation of the ferrite. This anisotropy of the microstructure must be taken into account when defining a representative model. The conducted numerical examples show that a mesomodel with 4 different cementite orientations and 16 crystallographic orientations (combined to give a mesomodel with 64 colonies with unique combinations of these orientations) give a representative model.

To overcome the limitations of using a 2D model future work will focus on a representative 3D model of pearlite. Furthermore, attention will be given to the issue of how to identify the material parameters of the constituents. Also, in order to study size effects (e.g. lamella distance dependence) it would be interesting to extend the current constitutive framework to a gradient-enhanced crystal plasticity model.

6 Acknowledgements

References

Ahlström, J.; Karlsson, B.: Fatigue behaviour of rail steel—a comparison between strain and stress controlled loading. *Wear*, 258, 7-8, (2005), 1187 – 1193.

Asaro, R. J.: Micromechanics of crystals and polycrystals. vol. 23 of *Advances in Applied Mechanics*, pages 1 – 115, Elsevier (1983).

Callister, W.: *Materials science and engineering - an introduction*. Wiley (2003).

Chang, Y.; Asaro, R.: An experimental study of shear localization in aluminum-copper single crystals. *Acta Metallurgica*, 29, 1, (1981), 241 – 257.

Ekh, M.; Lillbacka, R.; Runesson, K.: A model framework for anisotropic damage coupled to crystal (visco)plasticity. *International Journal of Plasticity*, 20, 12, (2004), 2143 – 2159.

Elwazri, A.; Wanjara, P.; Yue, S.: The effect of microstructural characteristics of pearlite on the mechanical properties of hypereutectoid steel. *Materials Science and Engineering: A*, 404, 1-2, (2005), 91 – 98.

Feyel, F.; Chaboche, J.-L.: Fe2 multiscale approach for modelling the elastoviscoplastic behaviour of long fibre sic/ti composite materials. *Computer Methods in Applied Mechanics and Engineering*, 183, 3-4, (2000), 309 – 330.

Hall, E.: The deformation and ageing of mild steel: III discussion of results. *Proc. Phys. Soc.*, 64, (1951), 747–753.

Havner, K.: *Finite plastic deformation of crystalline solids*. Cambridge University Press, Cambridge (1992).

Hill, R.: Elastic properties of reinforced solids: Some theoretical principles. *Journal of the Mechanics and Physics of Solids*, 11, 5, (1963), 357 – 372.

Hill, R.; Havner, K.: Perspectives in the mechanics of elastoplastic crystals. *Journal of the Mechanics and Physics of Solids*, 30, 1-2, (1982), 5 – 22.

Hu, X.; Houtte, P. V.; Liebeherr, M.; Walentek, A.; Seefeldt, M.; Vandekinderen, H.: Modeling work hardening of pearlitic steels by phenomenological and taylor-type micromechanical models. *Acta Materialia*, 54, 4, (2006), 1029 – 1040.

Hutchinson, J. W.: Elastic- plastic behavior of polycrystalline metals and composites. *Proc. Roy. Soc. Ser. A Math. Phys. Sci.*, 319, 1537, (1970), 247–272.

Johansson, G.; Ahlström, J.; Ekh, M.: Parameter identification and modeling of large ratcheting strains in carbon steel. *Computers and Structures*, 84, 15-16, (2006), 1002 – 1011.

Johansson, G.; Ekh, M.: On the modeling of evolving anisotropy and large strains in pearlitic steel. *European Journal of Mechanics - A/Solids*, 25, 6, (2006), 1041 – 1060.

Kocks, U.: The relation between polycrystal deformation and single-crystal deformation. *Metallurgical and Materials Transactions B*, 1, (1970), 1121–1143.

Kocks, W.: Thermodynamics and kinetics of slip. *Progr. Mater. Sci.*, 19, (1975), 291.

Kouznetsova, V.; Geers, M.: A multi-scale model of martensitic transformation plasticity. *Mechanics of Materials*, 40, 8, (2008), 641 – 657.

Long, X.; Peng, X.; Pi, W.: A microstructure-based analysis of cyclic plasticity of pearlitic steels with hill's self-consistent scheme incorporating general anisotropic eshelby tensor. *Acta Mechanica Sinica*, 24, (2008), 91–99.

Lubarda, V. A.: On the partition of rate of deformation in crystal plasticity. *International Journal of Plasticity*, 15, 7, (1999), 721 – 736.

Lundgren, J.; Rönnqvist, M.; Värbrand, P.: *Optimization*. Studentlitteratur, Lund, Sweden (2010).

Mehl, R.: The decomposition of austenite by nucleation and growth processes. *JISI*, 159, (1948), 113–129.

Miehe, C.; Schröder, J.; Schotte, J.: Computational homogenization analysis in finite plasticity simulation of texture development in polycrystalline materials. *Computer Methods in Applied Mechanics and Engineering*, 171, 3-4, (1999), 387 – 418.

Petch, N.: The cleavage strength of polycrystals. *J. Iron Steel Inst.*, 174, (1953), 25–28.

Simo, J.: Numerical analysis and simulation of plasticity. In: P. Ciarlet; J. Lions, eds., *Numerical Methods for Solids (Part 3) Numerical Methods for Solids (Part 3)*, vol. 6 of *Handbook of Numerical Analysis*, 183 – 499 (2004).

Toribio, J.; Ayaso, F.: Anisotropic fracture behaviour of cold drawn steel: a materials science approach. *Materials Science and Engineering: A*, 343, 1-2, (2003), 265 – 272.

Wetscher, F.; Stock, R.; Pippan, R.: Changes in the mechanical properties of a pearlitic steel due to large shear deformation. *Materials Science and Engineering: A*, 445-446, 0, (2007), 237 – 243.

Zhou, D.; Shiflet, G.: Ferrite: Cementite crystallography in pearlite. *Metallurgical and Materials Transactions A*, 23, (1992), 1259–1269.

Address: Erik Lindfeldt and Magnus Ekh, Department of Applied Mechanics, Division of Material and Computational Mechanics, Chalmers University of Technlogy, Gothenburg.
email: erik.lindfeldt@chalmers.se; magnus.ekh@chalmers.se